



# Hole annihilation vs. induced convection: Breakdown of different contributions to the photocorrosion mechanism of oxide-covered iron

Håvard Wilson, Svein Sunde, Andreas Erbe \*

Department of Materials Science and Engineering, NTNU, Norwegian University of Science and Technology, 7491 Trondheim, Norway

## ARTICLE INFO

### Keywords:

Iron  
Polarisation  
Passivity  
Anodic films  
Alkaline corrosion  
Passive films

## ABSTRACT

The mechanism behind corrosion rate increase of anodised iron under illumination has been studied by comparing photocurrents with corrosion currents from polarisation curves under controlled convection. Under illumination with photon energies larger than the iron oxide band gap of  $\sim 2$  eV, corrosion current densities increased by maximum 30%, triggered largely by hole annihilation through cation dissolution. Thermal effects in the oxide also play a role. Photocurrent measurements indicate little upward band bending, with fluctuations, in the n-type oxide at open circuit. The contributions of different mechanisms to the photocorrosion rate have been quantified, relevant for steels and photoelectrochemical water splitting.

## 1. Introduction

An increase of corrosion rates with illumination was observed already more than a century ago for iron in alkaline electrolytes [1,2]. Later, ultraviolet (UV) and blue light were found to “activate” the metal surface for photocorrosion, as opposed to red and infrared light [3]. The photoactivity of the iron corrosion products was then recognised, via their semiconducting properties [4,5]. Thus, increased corrosion rates under illumination were related to the photoactivation of semiconducting oxide corrosion products [6,7].

UV irradiation for up to 6 months has shown to increase weight loss for some metals like zinc, carbon steel, aluminium, copper and silver when immersed in running water [8]. No effect or a decreased weight loss compared to the control was found for titanium, aluminium, nickel and 304 stainless steel. The Gerischer model for charge transfer at semiconductor electrodes was therefore adapted and it was postulated — without experimental evidence to that end — that the holes from electron–holes pairs created during illumination annihilated via dissolution of the metal oxide [8].

However, this explanation is not universally accepted, as several different variants of the semiconductor model have been proposed. Most of these models attribute the effect of light on the corrosion process to an interaction with photoactive metal oxides. Pitting corrosion on iron is inhibited when illuminated [9–11]. One explanation is based on a passivation by hydroxyl radicals, formed in the reaction of electron–hole pairs with  $O_2$  [10,11]. An alternative explanation is based on the point

defect model (PDM) [12,13], suggesting the “photo-quenching” of the electric field driven vacancy movement as the mechanism behind the photo-inhibition of passivity breakdown [9]. Several works on illumination-triggered acceleration of uniform corrosion for iron, mild steels and weathering steels have been published [14–22]. While there is an agreement on the increase in corrosion rate during illumination, the proposed mechanisms differ. Photocorrosion of weathering steel is of particular interest [16–18,23], as corrosion resistance of this type of steel depends on the created corrosion products.

The photoconductivity of iron oxide corrosion products has been evidenced by electrochemical impedance spectroscopy, holes have been hypothesised to migrate to the oxide/electrolyte interface and the increased generation of oxyl radical species during the reaction between holes and water has been postulated to contribute to the observed increased corrosion rates [16]. A series of recent works [17,18,20,21, 23] proposes that the holes migrate toward the metal/oxide interface, as a result of downward band bending in the oxide. The experimental result this mechanism is based on was an observed increase in open circuit potential (OCP) when illuminating samples, interpreted as a “positive photo-voltage”. A photocorrosion mechanism was proposed specifically for weathering steels in NaCl solutions in which electrons migrate to the oxide/electrolyte interface and reduce  $O_2$  while holes oxidise the metal at the metal/oxide interface [18,20]. Additionally, it was postulated that holes would facilitate adsorption of  $Cl^-$ , leading to the formation of  $FeCl^+$  [18]. This model relies on downward band bending for n-type semiconductors, opposite to some other models [8]. While some authors

\* Corresponding author.

E-mail address: [fe-photocorrosion@the-passivists.org](mailto:fe-photocorrosion@the-passivists.org) (A. Erbe).

<https://doi.org/10.1016/j.corsci.2021.109426>

Received 29 November 2020; Received in revised form 18 February 2021; Accepted 24 March 2021

Available online 27 March 2021

0010-938X/© 2021 The Author(s). Published by Elsevier Ltd. This is an open access article under the CC BY license (<http://creativecommons.org/licenses/by/4.0/>).

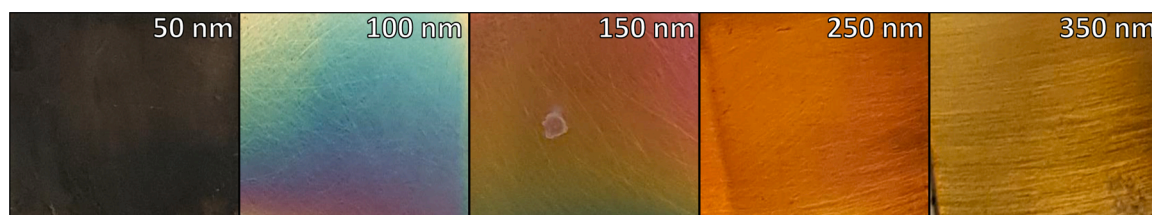


Fig. 1. Photos of the iron samples after anodisation. The samples are in order of increasing  $d$  from left to right. The thickness is indicated in the respective panel.

see the positive OCP shift as evidence for downward band bending [18, 20], an increase in OCP by illumination may also be explained by increased convection caused by localised heating [24].

Illumination affects the type of corrosion products formed on iron [7, 20], and can also transform already formed corrosion products [25,26]. The transformation of corrosion products is interesting, especially if the oxygen reduction reaction is the main cathodic reaction, because oxide composition and electronic structure affect the rate of the corrosion reaction on iron [27]. A reaction path was proposed in which the rate determining step is the adsorption of oxygen to active  $\text{Fe}^{2+}$  sites [28].

Some work has been carried out investigating the effect of sunlight irradiation on cathodic protection of steel [15,19]. An increase in current requirement was attributed to local heating which increased the rate of oxygen transfer to the metal surfaces [15,19]. The magnitude of this effect was judged to be too small to be of significant practical relevance [19]. Illumination causes localised heating in the Nernst diffusion layer, facilitating convection perpendicular to the surface and thus increasing oxygen reduction limiting currents [15,19,24].

Photocorrosion is also potentially problematic in photoelectrochemical processes, such as photoelectrochemical water splitting. Iron oxides have been successfully used as photoanodes in photoelectrochemical water splitting [29–31]. However, attention to stability issues is typically only secondary in this field. On the other hand, the importance of photocorrosion as limiting factor for the practical use of photoelectrochemical water splitting has been realised early on [32].

The different reported mechanisms for increased corrosion rates in virtually the same system under similar conditions serve as a motivation for a deeper look into the photocorrosion mechanism of iron. The reported mechanisms are based on photoelectrochemical processes with (i) upward and (ii) downward band bending in the oxide, or (iii) increased  $\text{O}_2$  transport. To clarify qualitatively the acting mechanisms, anodised iron samples with oxide thickness  $d$  up to 350 nm have been prepared, and illumination-dependent electrochemical behaviour has been analysed by polarisation curves, dissolution quantification, transient experiments and wavelength-dependent photoelectrochemical experiments. A second aim of this work is to quantify the contributions of the various processes by which illumination affects the corrosion of iron. To that end, we will employ anodised iron as a relatively well-

defined model system for iron corrosion products, though it is understood that corrosion product composition and thus the corresponding electronic structure is typically much more involved in “real-world” systems. For the discussion below we find it useful to define a net photocorrosion current density  $\Delta i_{\text{corr}}^{(\text{photo})}$  as difference between the corrosion current densities  $i_{\text{corr}}^{(\text{light})}$  in the presence and  $i_{\text{corr}}^{(\text{dark})}$  in the absence of illumination,

$$\Delta i_{\text{corr}}^{(\text{photo})} = i_{\text{corr}}^{(\text{light})} - i_{\text{corr}}^{(\text{dark})}, \quad (1)$$

where  $\Delta i_{\text{corr}}^{(\text{photo})}$  may be negative in the case of photoinhibition. Below we will also utilise the fact that the corrosion current density  $i_{\text{corr}}^{(\text{light})}$  for the illuminated sample in Eq. (1), in general, depends on the wavelength and intensity of illumination.

## 2. Materials and methods

Data from this study is available online [33].

### 2.1. Sample preparation

Plates of ARMCO Pure Iron, grade 4 (99.9% iron), were cleaned and polished to a mirror finish. The exposed area during experimentation was  $2.0 \text{ cm}^2$ . Samples were then either tested with the mirror finish, or further treated by an anodisation process to create thin oxide films on the iron surface.

Anodisation was chosen as a low-temperature preparation technique over thermal or gas phase deposition techniques as the results are perceived to be closer to corrosion products from aqueous solutions; differences between thermally and electrochemically grown oxide films have been reported [34]. Anodisation was conducted by potentiostatic polarisation with a DC N5771A power supply, for up to 10 min at either 1.5, 2.0 or 3.0 V, using a titanium plate  $5\times$  the surface area of the iron as cathode. The samples were anodised in a 12 M NaOH solution that was heated to  $70^\circ\text{C}$  using a water bath. This process is described in detail elsewhere [35,36].

The approximate thickness of the oxides could be determined by the anodising charge at the different potentials and exposure times;  $d$  was in the range 50–350 nm and was estimated from the oxide colours as described by Burleigh et al. [35]. Fig. 1 shows a photo of the samples after anodisation. It should be stressed that these thicknesses are estimates, and not quantitatively determined. Slight deviations of the colour towards the edge indicate differences in thickness. Such thickness differences would not affect uniform corrosion, they will only smear out the thickness effects on currents. Effects on the length scale of several millimetre, over which the surfaces may be not completely uniform, are not discussed in this work.

A detailed characterisation study of oxides prepared via exactly the same protocol is available elsewhere [36]. Here, oxides were characterised by grazing incidence X-ray diffraction (GIXRD) and Raman spectroscopy. Resulting diffractograms are very similar to those reported in the literature [36]. The Raman spectra closely resemble the spectra of  $\gamma\text{-Fe}_2\text{O}_3$  (maghemite) [25,37], whereas GIXRD patterns are similar to  $\text{Fe}_3\text{O}_4$  (magnetite). Because of the structural similarities between  $\gamma\text{-Fe}_2\text{O}_3$  and  $\text{Fe}_3\text{O}_4$ , a distinction has been difficult [36]; it can be

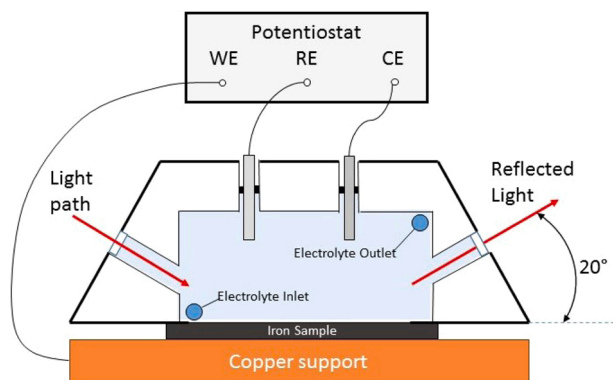


Fig. 2. Scheme of the experimental setup. Pure iron is supported by copper and illuminated with monochromatic light through a UV fused silica window.

concluded that anodised films consist of a strongly Fe<sup>II</sup>-deficient Fe<sub>3</sub>O<sub>4</sub> which is close to  $\gamma$ -Fe<sub>2</sub>O<sub>3</sub>. To determine the exact composition was beyond the scope of this work and would most likely strongly depend on the oxygen partial pressure during handling, see e.g. [38,39].

There can be large differences between the OCP of polished and anodised iron, if the surface finish was not exactly the same. Therefore, great care was taken to be consistent when polishing and anodising the samples.

## 2.2. Photoelectrochemical flowcell

To investigate photocorrosion of iron, samples of iron and iron oxide were placed into a custom-made flow cell to facilitate illumination and UV–visible (UV–VIS) spectroscopy in combination with electrochemical measurements. The cell (Fig. 2) is based on a design previously used for in situ spectroscopic measurement [40,41]. The cell house was made from PTFE while a support made of copper was utilised to obtain electrical contact with the samples. The contact area with electrolyte is 10 mm × 20 mm. The samples were illuminated at an angle of incidence of 70° through a flat UV fused silica high precision window. The angle of incidence was chosen to deliver high intensities of light near to the metal surface, in analogy to the “surface selection rule” known from analytic spectroscopy [42]. This large angle of incidence also ensures a homogeneous illumination of the majority of the sample surface; the illuminated area equals approximately the full sample area. The angle of incidence was not varied in this study. A Newport 6258 300 W xenon arc lamp (spectral range 260–1000 nm) was used as light source. The power density, taking into account reflection losses at the entrance windows, would be on the order of 100 W cm<sup>-2</sup>. For the wavelength specific experiments, an Oriel Cornerstone 260 Monochromator was used, providing monochromatic light with approximately 10 nm spectral width.

Electrochemical measurements were obtained using a standard three electrode setup and a Zahner IM6e potentiostat. The electrode potential was measured versus a DRIREF-2 Ag/AgCl/3 M KCl reference electrode. All electrode potentials in this work are reported against this reference electrode (+210 mV vs. standard hydrogen electrode), unless noted otherwise. Coiled platinum wire was used as a counter electrode.

The electrolyte was pumped into the chamber from the bottom, using a Harvard Syringe Pump 33, with a 50 mL syringe. A flow rate of 0.5 mL min<sup>-1</sup> was used, which replenishes all of the electrolyte in the test chamber every 4 min. The flow rate was chosen as a compromise between keeping the chamber cool, while also inciting as little noise as possible. The electrolyte exits the chamber through an outlet at the top of the cell, ensuring that the entire sample is immersed during the entire experiment.

To monitor any heating effects, a Fluke 53II B thermometer was used to measure the surface temperature during illumination before any electrochemical measurements were carried out. A thermocouple was placed in contact with the sample surface to quantify any local heating effects from illumination. The temperature was recorded before, after and during illuminating of the sample exposed to flowing electrolyte. The temperature increased by maximum 0.2 °C, after 5 min of illumination.

## 2.3. Electrochemical measurements

The samples were kept in the cell at OCP for 10–20 min in the dark until the potential stabilised; in NaCl solution no stabilisation was observed and measurements were started after 40 min. As a criterion for a stable potential, a drift of less than 1 mV during 2 min was used. Illumination was started no more than 10 s before the polarisation curves were started. All measurements with polished, non-anodised samples were done with 5 repeats both in the dark and with illumination. For anodised samples, 3 repeats were carried out. Uncertainty estimates (single standard deviation) are given for the last digit of the

respective quantity in brackets behind the average.

Five different electrolytes were used for the polished samples: 0.1 M NaOH, borate buffer (0.05 M Borax, 0.2 M boric acid, pH 9), unbuffered 3.5 wt% NaCl ( $\approx$ 0.6 M; pH  $\approx$ 7), 0.001 M H<sub>2</sub>SO<sub>4</sub> (pH  $\approx$ 5) and 0.01 M H<sub>2</sub>SO<sub>4</sub> (pH  $\approx$ 2). NaCl was used for easier comparison with literature work. All electrolytes were made using analytical grade chemicals. Only 0.1 M NaOH was used for the anodised samples, as the oxide film dissolved in the more acidic electrolytes.

For the potentiodynamic polarisation curves, an interval of  $\pm$ 300 mV around OCP was used, with a linear scan from negative to positive potential, with scan rate of 1 mV s<sup>-1</sup>. The scan rate from OCP to the most negative potential, which also marked the starting potential for the polarisation curves, was 10 mV s<sup>-1</sup>. The corrosion potentials determined from polarisation curves are denoted as  $E_{\text{corr}}$  in this work, to distinguish them from the measurements of the OCP.

Mott–Schottky analysis was performed for polished iron and anodised iron in 0.1 M NaOH to find semiconductor properties of the oxides on the sample. The corresponding impedance experiments were conducted from –1.0 to 0.4 V vs. Ag/AgCl/3 M KCl in 10 mV intervals, between 1 kHz and 1 Hz. Mott–Schottky plots above 1 kHz were too noisy for systematic analysis.

Photocurrents, and respective photocurrent densities  $i_{\text{photo}}$ , were obtained by chronoamperometry in 0.1 M NaOH, while the sample was illuminated with white or monochromatic light for 10 s. Mostly, steady state values of  $i_{\text{photo}}$  will be quantitatively compared. Photovoltages were obtained by recording the OCP while illuminating the samples with white light or monochromatic light for durations of up to several tens of seconds.

For 0.1 M NaOH, the experiment was performed for both the anodised and polished samples. In addition to experiments with immediate start after setting up, the polished samples were also anodically polarised to 200 mV vs. Ag/AgCl/3 M KCl (approximately 425 mV above OCP) in 0.1 M NaOH for 1, 2, 4 and 6 h before the chronoamperometry was performed, to investigate if the natural oxide that develops in the electrolyte also is photoactive.

## 2.4. UV–VIS spectroscopy

### 2.4.1. UV–VIS reflectance measurements

Ex situ UV–VIS spectroscopy was performed to find the optical band gap of the oxides formed on the iron. These experiments were done using an integrating sphere and a xenon arc lamp as a light source, without the presence of electrolyte. Optical fibres were used to direct the light from the light source into the integrating sphere and from the integrating sphere to a Avantes AvaSpec-2048 spectrometer for spectrum analysis. Polished aluminium foil was used as a reference for the calculation of absorbance.

### 2.4.2. Quantification of dissolved iron

UV–VIS spectroscopy of the solution was used to quantify the concentration of dissolved iron in electrolyte downstream after the electrochemical cell, based on an established method [43]. A standard series was made by dissolving 0.1171 g of 99.8% iron sponge from Alfa Aesar in 1.0 mL hot concentrated HCl. When the iron was completely dissolved, the solution was filled to 1000 mL with distilled water. The resulting Fe<sup>2+</sup> solution was further diluted to a 10<sup>-5</sup> M solution, which was used to create a series of different iron concentrations between 1 × 10<sup>-7</sup> and 2 × 10<sup>-6</sup> M by transferring different volumes of standard concentration to 100 mL flasks. 1 mL of 0.3 M hydroxylamine hydrochloride was added to reduce any Fe<sup>3+</sup> to Fe<sup>2+</sup>, 5 mL of 1.2 M sodium acetate were added to regulate the pH, and 5 mL of 1,10-phenanthroline were added to the 100 mL flasks for formation of a complex with Fe<sup>2+</sup>. This complex is strongly light-absorbing in the visible. The solution was then then diluted to 100 mL with distilled water.

UV–VIS absorbance was then performed on the standard series. A solution of 1 mL of 0.3 M hydroxylamine hydrochloride, 5 mL of 1.2 M

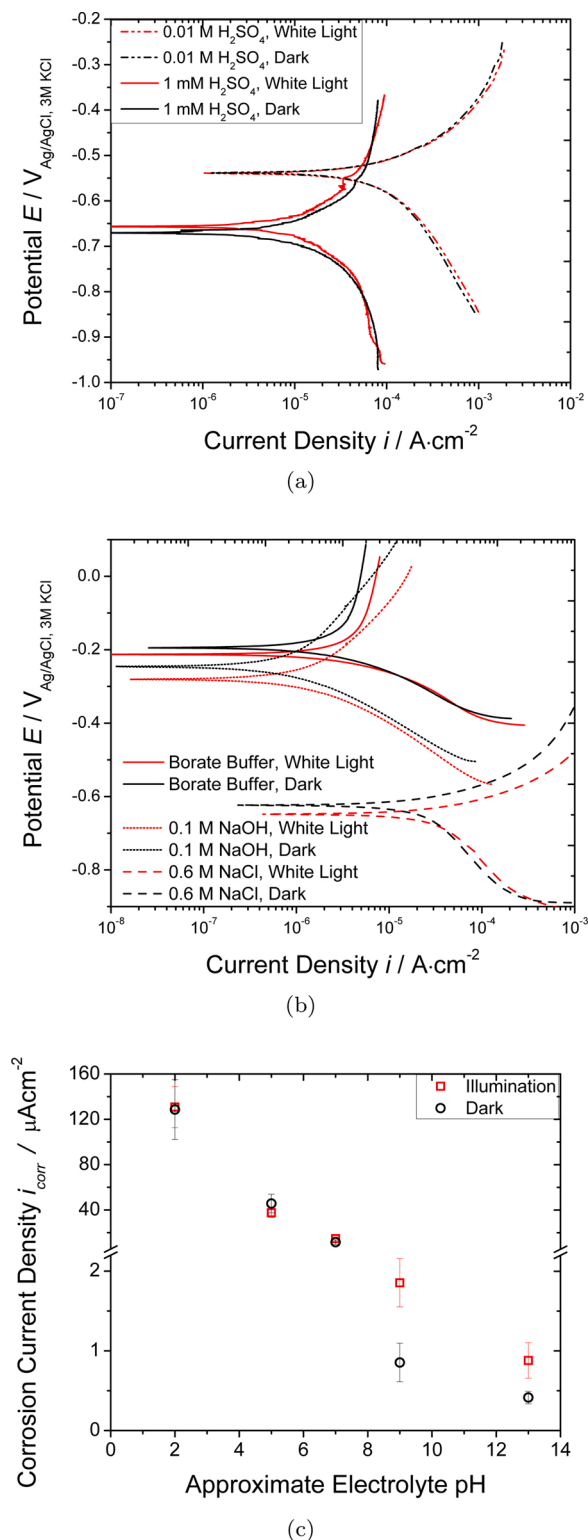


**Fig. 3.** Polarisation curves for polished iron in different electrolytes in the dark and under illumination with white light, in (a) 0.1 M and 0.001 M H<sub>2</sub>SO<sub>4</sub>, (b) 0.6 M NaCl, borate buffer and 0.1 M NaOH. (c) Comparison of corrosion current densities for dark and illuminated iron for different electrolyte pH.

sodium acetate and 5 mL of 1,10-phenanthroline then diluted to 100 mL with distilled water was used as a reference.

The largest absorbance was measured at 515 nm wavelength for the  $2 \times 10^{-6}$  M solution. For the  $1 \times 10^{-7}$  M solution, no peak was found at 515 nm; this concentration is therefore considered the detection limit.

**Table 1**

Electrochemical parameters extracted from polarisation curves (Fig. 3) for polished iron in different electrolytes, comparing illuminated and unilluminated samples:  $E_{corr}$ ,  $i_{corr}$ , apparent anodic and cathodic Tafel slopes,  $b_c$  and  $b_a$ , respectively. No values are given for  $b_a$  in 0.001 M H<sub>2</sub>SO<sub>4</sub> as no linear region existed.

	$i_{corr}$ ( $\mu A \cdot cm^{-2}$ )	$E_{corr}$ (mV)	$b_c$ (mV dec. <sup>-1</sup> )	$b_a$ (mV dec. <sup>-1</sup> )
Illumin. (0.01 M H <sub>2</sub> SO <sub>4</sub> )	119(4)	-527(8)	-389(35)	157(6)
Dark (0.01 M H <sub>2</sub> SO <sub>4</sub> )	116(11)	-535(7)	-352(23)	154(10)
Illumin. (0.001 M H <sub>2</sub> SO <sub>4</sub> )	38(4)	-621(4)	-753(124)	–
Dark (0.001 M H <sub>2</sub> SO <sub>4</sub> )	46(8)	-607(20)	-846(168)	–
Illumin. (NaCl)	16(3)	-636(18)	-290(34)	103(15)
Dark (NaCl)	12(2)	-609(25)	-276(26)	103(19)
Illumin. (Borate)	1.9(3)	-242(20)	-165(18)	515(78)
Dark (Borate)	0.8(0)	-218(12)	-133(6)	480(79)
Illumin. (NaOH)	0.9(2)	-281(1)	-167(25)	278(53)
Dark (NaOH)	0.4(1)	-255(13)	-177(11)	314(13)

Absorbance was then plotted vs. concentration. The resulting linear trend line with an absorption coefficient of  $\approx 3.4 \times 10^4 L \cdot mol^{-1} \cdot cm^{-1}$  was then used to calculate the Fe<sup>2+</sup> concentration in the exposed electrolyte.

Six samples of anodised iron were left at OCP, three of them in the dark and three under white illumination. The samples were then exposed to an electrolyte with a flow rate of  $0.1 mL \cdot min^{-1}$  for 2.5 h. 1 mL of 0.3 M hydroxylamine hydrochloride, 5 mL of 1.2 M sodium acetate and 5 mL of 1,10-phenanthroline were added to the solution, and UV-VIS absorbance was measured. The absorbance at 515 nm was recorded and used to determine the Fe<sup>2+</sup> concentration.

As the volume of electrolyte, exposure time and iron concentration was known, an estimate of the corrosion current density was calculated from the dissolved iron concentration.

### 3. Results

#### 3.1. Polarisation curves

Typical linear polarisation curves of polished iron with and without white illumination are shown in Fig. 3, and a comparison of the key values from 5 different samples is compiled in Table 1. The linear regions of these polarisation curves — as well as those shown further below — do not extend for more than maximum one decade. For iron in 0.01 and 0.001 M H<sub>2</sub>SO<sub>4</sub>, no significant difference with illumination was found; any difference in current density was within the standard deviation. However, for NaCl, NaOH and borate buffer solutions, an increase in corrosion current density was found upon illuminating the sample. For iron,  $i_{corr}$  in 0.1 M NaOH and borate buffer increased from 0.4(1) to 0.9(2)  $\mu A \cdot cm^{-2}$  and from 0.8(0) to 1.9(3)  $\mu A \cdot cm^{-2}$ , respectively.

The anodic current is slightly higher for the samples illuminated with white light, and  $E_{corr}$  is shifted to more negative values by illumination.

Typical polarisation curves of anodised iron in 0.1 M NaOH with and without white light illumination are shown in Fig. 4. A comparison of the electrochemical parameters from 3 different samples may be found in Table 2. The curves are similar to those for polished iron in 0.1 M NaOH, with a small increase in the anodic current and decrease in  $E_{corr}$  for the illuminated samples as compared to the dark. For all the anodised samples,  $i_{corr}$  increased when illuminated. Anodised iron was also tested



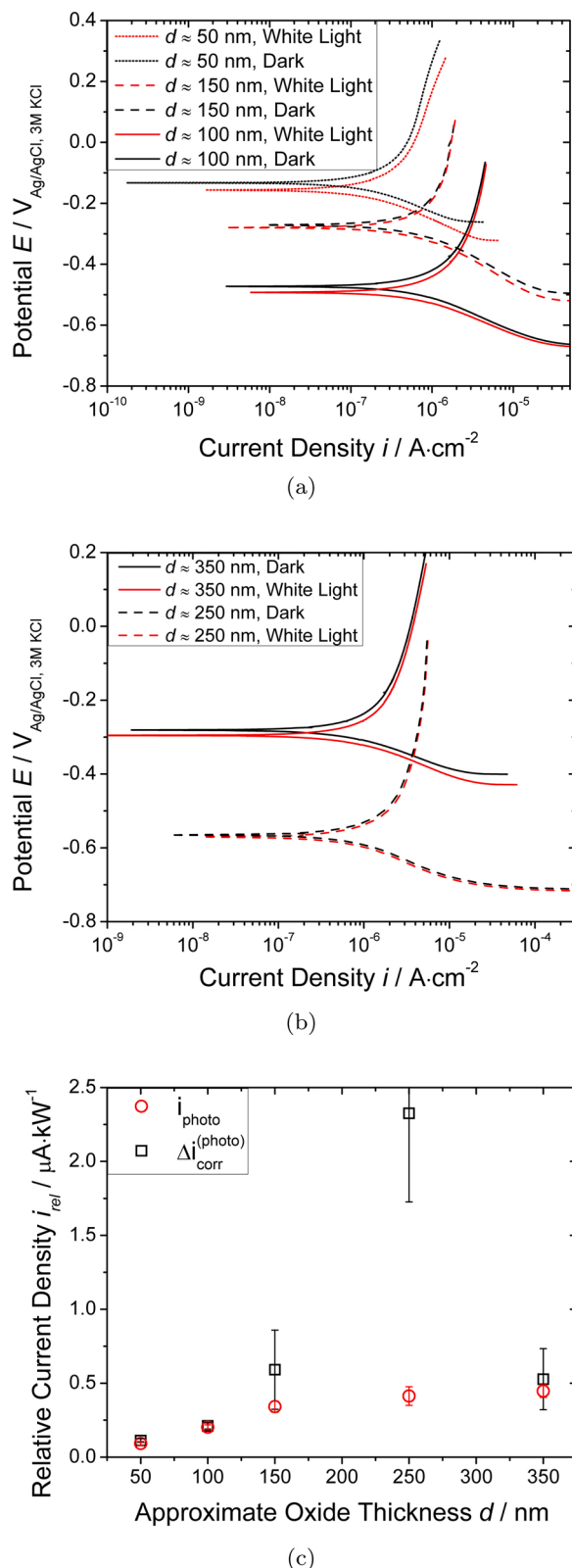


**Fig. 4.** Polarisation curves for unilluminated and white light illuminated anodised iron in 0.1 M NaOH; (a)  $d = 50, 100$  and  $150$  nm, (b)  $d = 250$  and  $350$  nm. (c) Comparison of  $\Delta i_{\text{corr}}^{(\text{photo})}$  and normalised white light photocurrent  $i_{\text{rel}}$ , obtained as  $i_{\text{rel}} = i_{\text{photo}}/P$ , with normalised illumination power  $P$  on the order of  $100 \text{ W cm}^{-2}$ . See Section 3.2 for  $i_{\text{photo}}$ .

**Table 2**

Parameters extracted from polarisation curves (Fig. 4) for anodised iron with different oxide thickness in 0.1 M NaOH.

$d$ (nm)		$i_{\text{corr}} (\mu\text{A cm}^{-2})$	$E_{\text{corr}}$ (mV)	$b_c$ (mV dec. $^{-1}$ )	$b_a$ (mV dec. $^{-1}$ )
50	Illumin.	0.145(1)	-144(7)	-118(2)	214(7)
	Dark	0.137(8)	-143(8)	-115(7)	220(11)
100	Illumin.	0.538(2)	-463(42)	-115(11)	197(0)
	Dark	0.517(3)	-491(25)	-107(9)	208(2)
150	Illumin.	0.65(3)	-276(5)	-152(5)	501(35)
	Dark	0.59(3)	-276(4)	-147(4)	454(7)
250	Illumin.	1.3(2)	-516(70)	-108(12)	204(64)
	Dark	0.9(2)	-575(13)	-83(9)	109(22)
350	Illumin.	0.59(3)	-289(5)	-88(3)	185(21)
	Dark	0.53(1)	-279(3)	-83(0)	190(1)

in NaCl and  $\text{H}_2\text{SO}_4$ , however, the oxides were not stable in these solutions and dissolved during exposure to the electrolytes. It was therefore not possible to investigate anodised iron in other electrolytes than alkaline.

Typical polarisation curves in 0.1 M NaOH for 250 nm thick iron oxide illuminated with monochromatic light of different wavelengths are shown in Fig. 5 and compared to polarisation curves recorded under dark conditions in the same figure. Key parameters are summarised in Table 3. An increase in anodic current is only noticeable from  $E_{\text{corr}}$  to approximately 200 mV above  $E_{\text{corr}}$ , but there is a distinct increased anodic current when illuminated, and a lower cathodic current below  $E_{\text{corr}}$ . This increase in anodic current is enough to increase the corrosion current density so that the increase is more than the standard deviation between samples.

### 3.2. Photoelectrochemical properties of oxide-covered iron

Typical photocurrent transients for anodised iron in 0.1 M NaOH are shown in Fig. 6a. When the light is turned on, a sudden increase in anodic current occurs, followed by a rapid decrease until the current reaches a steady-state value which is larger in magnitude than the dark current after 10–20 s. The steady state increase from dark to light current is between  $0.01$  and  $0.05 \mu\text{A cm}^{-2}$  for the thinnest and thickest oxide films, respectively. Turning the light off causes an immediate decrease in current; the current becomes cathodic. The current returns to zero after  $\approx 20$  s.

Fig. 6b shows the effect of illumination on the OCP of anodised iron in 0.1 M NaOH. When the sample is illuminated, the OCP rapidly decreases. This potential shift occurs in the opposite direction of what has been reported previously [17,18,20]. The effect is small, with only a 1 mV shift for the 350 nm thick oxide, and no effect was measured for the oxides thinner than 150 nm. An increase in current upon illumination was recorded for the anodised iron samples. The photocurrents recorded during exposure to monochromatic light in the range from 320 to 1000 nm (stepped in 10 nm intervals) are shown in Fig. 6c. The current increase is observed only for light with a photon energy above a certain threshold, and no current response was seen for light below this threshold.

The photon-energy threshold for photocurrent generation agrees with the band gap found from absorbance spectra and Tauc plots, an example of which is presented in Fig. 7 for a 350 nm thick oxide. Absorption increases for wavelengths shorter than 600 nm for the anodised samples, corresponding to a band gap of 2.2 eV found from the Tauc plot. The band gap varied slightly for the different thicknesses, between 1.9 and 2.2 eV for the thickest and thinnest oxides, respectively. The Tauc plot gives a linear relationship for an exponent of 2, indicating a direct band gap.

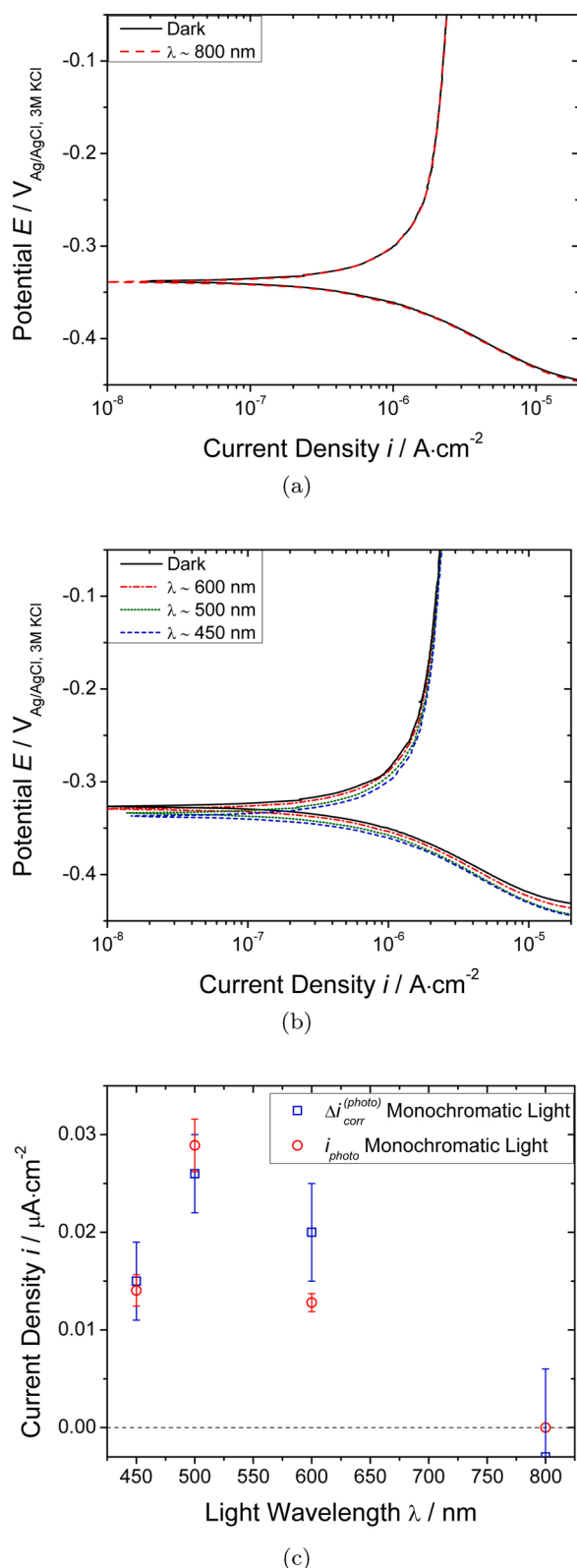


**Fig. 5.** Polarisation curves in 0.1 M NaOH for iron covered with a 250 nm thick iron oxide, comparing dark conditions and monochromatic illumination at photon energies of (a) less than the oxide band gap, 800 nm, and (b) higher than band gap, 600, 500 & 450 nm. (c) Comparison of  $\Delta i_{corr}^{(photo)}$  and monochromatic  $i_{photo}$ .

To evaluate whether the native corrosion product in 0.1 M NaOH also is photoactive, and not only the layers formed in hot concentrated NaOH, polished iron was exposed to 0.1 M NaOH solution and polarised to +200 mV above initial OCP up to 6 h. The shape of the current transient is similar to the anodised samples, but the measured  $i_{photo}$  is small compared to the anodised samples (Fig. 8). Only 4 and 6 h polarisation are shown here, as there was no noticeable  $i_{photo}$  for shorter polarisation.

A Mott–Schottky plot for anodised iron in NaOH is shown in Fig. 9a. The anodised iron had reproducible results for frequencies ranged 100–5 Hz, but showed no clear trend above 100 Hz. Only the result for the anodised iron is shown; for the polished samples, no reproducible, clear Mott–Schottky plot was obtained. In the plot, however, it is hard to find the typical linear region used for quantitative analysis. Therefore, for comparison  $i_{photo}$  experiments are shown in Fig. 9a which should verify at which potential the oxide becomes photoactive. The increasing  $i_{photo}$  with increasing electrode potential can be used to estimate a flat band potential of lower than  $-0.30$  V. Whereas an exponential potential dependence is expected [44], the experiments here follow approximately a linear dependence; linear regression indicates that the flat band potential (=onset potential for  $i_{photo}$ ) is approximately  $-0.35$  V.

### 3.3. Quantification of iron dissolution

Anodised iron with a 250 nm oxide was exposed for 2.5 h to 0.1 M NaOH, (i) in the dark and (ii) under white light illumination. UV–VIS spectroscopy (Section 2.4.2) showed no signal of  $Fe^{2+}$  for the samples in the dark, while the typical absorbance spectra obtained in the calibration experiments was recovered for illuminated samples. The average absorbance measured for the three samples exposed to white light corresponds to a solution concentration of  $1.0(1) \times 10^{-6}$  M  $Fe^{2+}$ , and based on a known electrolyte volume and exposure time, the iron concentration can be converted to dissolution current density of  $0.10(2) \mu A \cdot cm^{-2}$ . This value is not the total corrosion rate, but only the part of the corrosion rate related to dissolving iron. Additional current could contribute to grow of the iron oxide layer.

After exposure for 2.5 h, none of the samples showed any visible change in colour. Only parts of the anodised surface were exposed to the electrolyte. Any change in colour would then create a clear border between the non-exposed and exposed area, making even small changes in appearance detectable.

## 4. Discussion

### 4.1. Role of electron–hole pair formation

The results shown in Section 3 show that — under controlled convection — electron–hole pairs generated within a semiconducting iron oxide by exposing the sample to light are the main cause of  $\Delta i_{corr}^{(photo)}$ , because (i) a stable iron oxide film is needed for the observation of  $\Delta i_{corr}^{(photo)}$ , (ii)  $\Delta i_{corr}^{(photo)}$  agrees in most cases well with  $i_{photo}$ , (iii) both  $\Delta i_{corr}^{(photo)}$  and  $i_{photo}$  are observed at illumination with photon energies above the oxide band gap, and (iv) the inferred band bending is in agreement with the expectations for such a mechanism.

An iron oxide film on the iron surface is needed for  $\Delta i_{corr}^{(photo)} > 0$ . Iron without any oxide (acidic solutions) does not display any positive  $\Delta i_{corr}^{(photo)}$ . For passive iron with a stable oxide (alkaline solutions),  $\Delta i_{corr}^{(photo)} > 0$ .

The oxide displays semiconducting properties and is therefore prone to electron–hole pair generation upon exposure to light. The Mott–Schottky plot shows an n-type semiconductor with positive slopes, which is expected for iron oxides [45,46]. Typical Mott–Schottky plots of pure semiconductor crystals exhibit a more abrupt, linear increase in  $C^{-2}$ . For the oxide films in this study, in the potential region  $\approx -0.5$  to

**Table 3**

Electrochemical parameters extracted from polarisation curves (Fig. 5) for anodised iron with  $d = 250$  nm in 0.1 M NaOH, comparing unilluminated samples with samples illuminated with different wavelengths of monochromatic light. The value for the unilluminated sample is for control samples measured at the respective wavelength.

Monochromatic light (nm)		$i_{\text{corr}} (\mu\text{A cm}^{-2})$	$E_{\text{corr}} (\text{mV})$	$b_c (\text{mV dec.}^{-1})$	$b_a (\text{mV dec.}^{-1})$
450	Illumin.	0.601(6)	−337(1)	−77(1)	151(28)
	Dark	0.586(2)	−337(2)	−75(0)	166(3)
500	Illumin.	0.585(4)	−332(2)	−77(0)	158(7)
	Dark	0.559(6)	−330(1)	−75(1)	154(7)
600	Illumin.	0.579(7)	−328(1)	−75(0)	170(13)
	Dark	0.559(6)	−330(1)	−75(1)	154(7)
800	Illumin.	0.597(9)	−339(1)	−77(2)	185(6)
	Dark	0.593(11)	−338(2)	−76(2)	177(26)

0.4 V,  $C^{-2}$  increases non-linearly. Such nonlinearity is not uncommon [47–49], because of defect-related intragap states. The observation of  $i_{\text{photo}}$  down to −0.30 V indicates an upward band bending below 0.0 V

The behaviour of  $i_{\text{photo}}$  and that  $i_{\text{photo}}$  correlates with  $\Delta i_{\text{corr}}^{(\text{photo})}$  also support that the iron oxide has n-type semiconductor properties. There is a correlation between the oxide band gap and the photon energy required to generate a non-zero  $i_{\text{photo}}$ . If the band to band transition in the semiconductor oxide film is responsible for the measured  $i_{\text{photo}}$ , it should only occur when the illumination has photon energies above the band gap of the oxide film, in agreement with the results. The monochromatic  $i_{\text{photo}}$  response increases with increased absorption above the band gap, determined here as 1.9–2.2 eV. Additionally, only illumination of the stable oxide with light of photon energies above the band gap causes  $\Delta i_{\text{corr}}^{(\text{photo})} > 0$ . Illumination below the band gap does not affect the corrosion rate. Illumination shifted OCP of anodised iron to negative values, and the measured  $i_{\text{photo}}$  are anodic;  $i_{\text{photo}}$  can only be recorded at potentials above the flat band potential, as typical for an n-type semiconductor. At potentials above the flat band potential, the bands for an n-type semiconductor are bent upwards, and the holes would thus migrate towards the oxide-electrolyte interface.

There is thus no evidence for a downward band bending in the oxides around  $E_{\text{corr}}$  or OCP. Bands would typically be bent upward, though a very low degree of band bending may occur at potentials close to the flat band potential. With the very poor definition of the flat band potential in these systems, the band structure in the oxide layers must obviously be more involved than in the typical crystalline semiconductor. If the bands were bent upward, then a suppression of the cathodic reaction, e.g. the oxygen reduction in a typical corrosion process, would be expected, but no suppression was observed. On the other hand, if there was no appreciable band bending, a cathodic reaction would be possible, but no driving force for electron-hole pair separation would exist and thus no photocurrent — in clear violation to the observations. Here, we conclude that there must be some degree of band bending, but still on a level that fluctuations in the band bending enable a certain rate of a cathodic reaction on the same surface. Schematically, the band diagram is shown in Fig. 10. In a crystalline semiconductor, band bending is caused by the Fermi level alignment across the interface, e.g. [44]. In a corroding system with strongly disordered oxide and an ill-defined and variable solution Fermi level, it is reasonable to assume that the large variety of intragap states causes a mechanism of Fermi level alignment without the need for large scale carrier rearrangement that leads to a very structured space charge layer in the semiconducting oxide.

The dependence of the photocurrent on oxide thickness is also in agreement with a mechanism based on electron-hole pair formation, since a thin oxide would absorb fewer photons than a thick oxide. The largest  $\Delta i_{\text{corr}}^{(\text{photo})}$  was  $0.23 \mu\text{A cm}^{-2}$ , corresponding of a 30% increase of  $i_{\text{corr}}$  for the 250 nm thick oxide, however, with a large uncertainty.  $i_{\text{photo}}$  increased with oxide thickness, and was the highest for the 350 nm thick oxide. For most anodised oxide films,  $\Delta i_{\text{corr}}^{(\text{photo})} \approx i_{\text{photo}}$  (Fig. 4), except for the 250 nm sample, for which  $\Delta i_{\text{corr}}^{(\text{photo})} > i_{\text{photo}}$ . All the repeats with this

thickness showed higher  $\Delta i_{\text{corr}}^{(\text{photo})}$  than all other measurements, indicating indeed that this thickness behaves in a special way. The good agreement between  $\Delta i_{\text{corr}}^{(\text{photo})}$  and  $i_{\text{photo}}$ , with exception of the 250 nm oxide, is an indication that the increased corrosion current measured is indeed caused by the  $i_{\text{photo}}$ .

The photocurrent observed corresponds to a corrosion process, and more specifically a dissolution process. The corrosion current density in the dark is related to an oxide growth process, while the additional photocurrent is related to a dissolution process, because dissolved iron can be detected in the solution only when the sample is exposed to light.

Overall, a non-trivial thickness dependence of the light absorption in the oxide with  $d$  smaller than the wavelength is to be expected; in the vicinity of a metal surface, a standing wave pattern forms, with intensity minima and maxima at wavelength-dependent distances (see, e.g. [42, 50] and references therein for a discussion of the underlying physics). While a modelling of this effect on the basis of continuum electro-dynamics is straightforward for monochromatic light in a medium with known complex refractive index, the latter is not given for the oxide in the system investigated here. In addition a very accurate modelling of the spectral output of the lamp would be needed. Importantly, such a modelling wouldn't explain the differences between  $i_{\text{photo}}$  and  $\Delta i_{\text{corr}}^{(\text{photo})}$  for the 250 nm system and the absence of such a difference for the other thicknesses. Likewise, two photon absorption in a high intensity region near the oxide/solution interface would be expected to impact on both the  $i_{\text{photo}}$  as well as  $\Delta i_{\text{corr}}^{(\text{photo})}$ .

From this work, there is no evidence for a direct involvement of oxyl radicals, but such an involvement cannot be excluded. Electron-hole pairs could either directly dissolve the iron oxide, as has been proposed qualitatively earlier [8]; as an additional or alternative explanation it been postulated [10,11] that different oxyl radicals may form when illuminating, causing increased pitting resistance. Later it has been proposed that the same radicals also may increase general corrosion rate in weathering steels [16]. The results in this paper do not directly exclude this explanation. These radicals would form as intermediates in oxygen reduction or evolution [51,52], and an increased formation rate would require an increase in the cathodic reaction rate by illumination. We did not observe such an increase here. Hydroxyl radicals, however, may also form as result of a reaction between a hole and  $\text{OH}^-$  or  $\text{H}_2\text{O}$  at the oxide/electrolyte interface. In the system here, it is not obvious how radical formation would lead to an increased dissolution rate, and the effect of illumination on the cathodic processes also does not give any evidence of enhancement under illumination (Section 4.4).

Based on the PDM, and in line with the results from this work, a likely candidate reaction for the dissolution step is



In this step, the charge  $\delta$  of the resulting iron vacancy is not immediately obvious; it determines the number of holes that ejection of one  $\text{Fe}^{3+}$  ion would annihilate. Alternatively, the dissolution product may originate from iron interstitials; no vacancy would be generated in this case. The

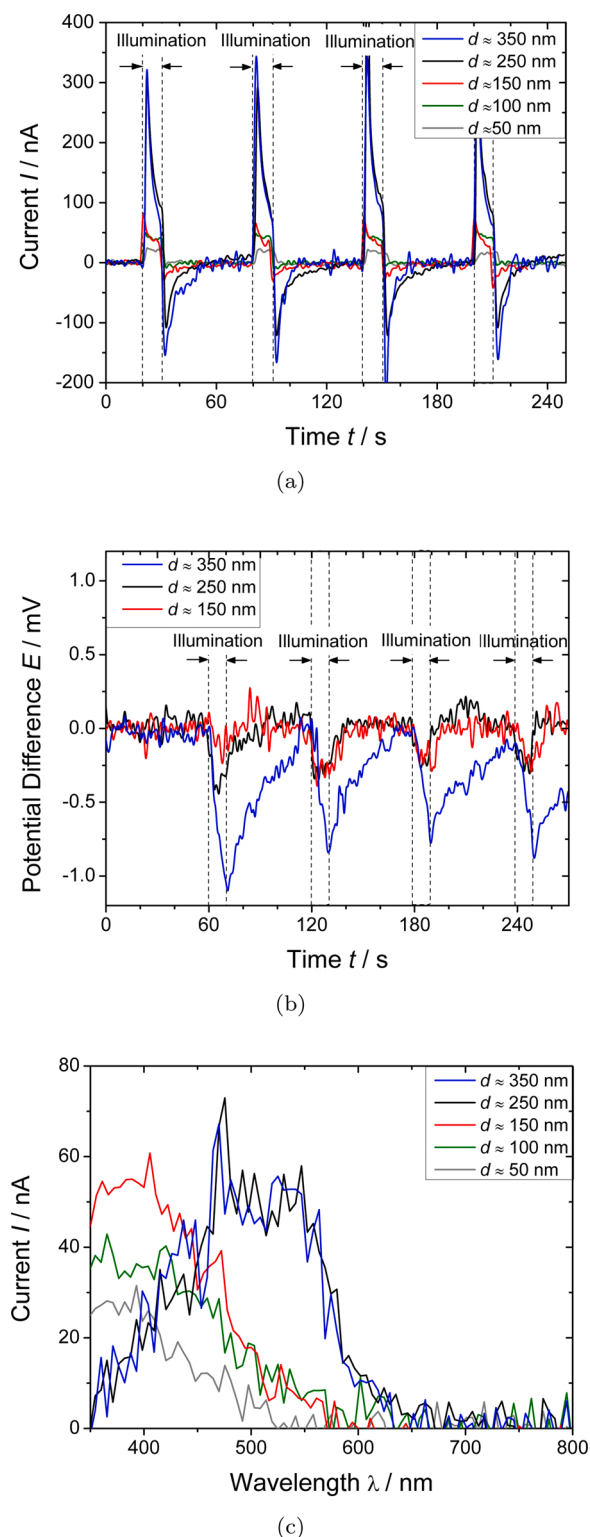


**Fig. 6.** Transient photocurrent and photovoltage for anodised iron in 0.1 M NaOH. (a) Transient photocurrent from white light for different iron oxide thickness, polarised to original OCP. (b) Transient photovoltage (displayed as potential difference to dark OCP) caused by white light for different iron oxide thicknesses. (c) Transient photocurrent from monochromatic light illumination with wavelengths from 800 to 350 nm for different iron oxide thicknesses, polarised to original OCP.

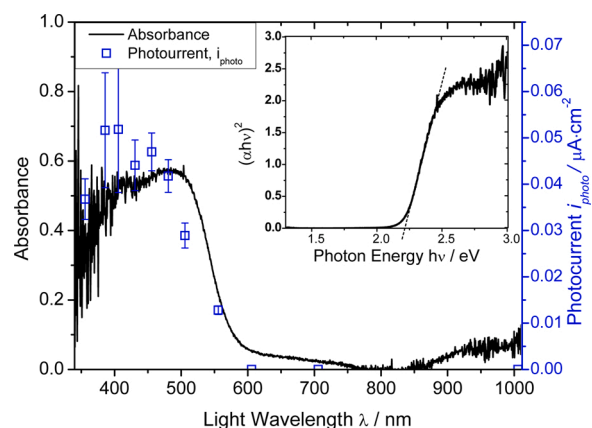


**Fig. 7.** Photocurrents at different wavelengths for 350 nm thick iron oxide in 0.1 M NaOH compared to the absorbance spectrum. Inset: Corresponding Tauc plot obtained ex situ with an integrating sphere. Dotted line represents fit to the linear region, yielding an oxide band gap of  $\approx 2.2$  eV.

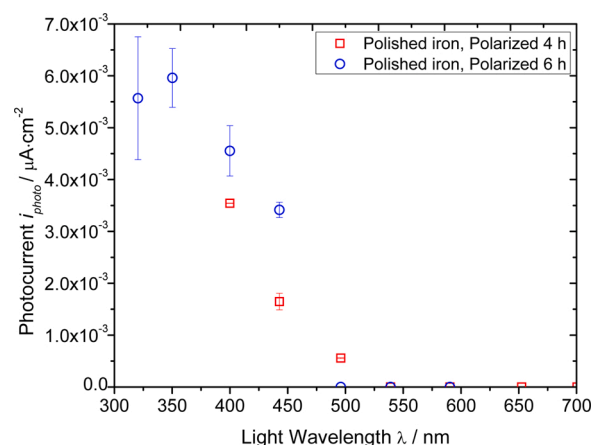


**Fig. 8.** Photocurrents for polished iron under monochromatic illumination after polarisation to +200 mV vs. Ag/AgCl/3 M KCl (+400 mV vs. initial OCP) for 4 and 6 h in 0.1 M NaOH. No photocurrent was found for the samples polarised shorter than 4 h.

corresponding electron from the electron–hole pair would participate in the cathodic reaction; iron oxidation would happen at the metal/oxide interface. The formation of  $Fe^{3+}_{(aq)}$  in this mechanism relies on the dominance of  $Fe^{III}$  in the lattice of the oxide. A corresponding dissolution step leading to  $Fe^{2+}_{(aq)}$  from the  $Fe^{II}$  fraction of the oxide can be easily formulated. However, in this mechanism, the dissolving product is the dominating ion in the oxide, whereas in the typical active corrosion of iron,  $Fe^{2+}_{(aq)}$  is formed in the first dissolution step. Photocorrosion according to such a mechanism should thus yield a larger amount of  $Fe^{3+}_{(aq)}$  in solution than corrosion without illumination. In this work, due to a number of practical difficulties, the ratio between  $Fe^{2+}_{(aq)}$  and  $Fe^{3+}_{(aq)}$  hasn't been determined. However, an analysis of this ratio could be used to collect experimental evidence for reaction (2).

We cannot exclude the possibility that part of the observed photocurrent is caused by side reactions. The anodic current generated by illumination is often associated with photoelectrolysis of water, which yields either  $O_2$  or  $H_2O_2$  [34,53–55]. However, the detection of dissolved iron in the solution shows that a non-zero fraction of the photocurrent is related to corrosion and dissolution of an iron oxide. The fast initial current transient of  $i_{photo}$  is further evidence for a semiconductor electrochemical process. This increase is followed by a



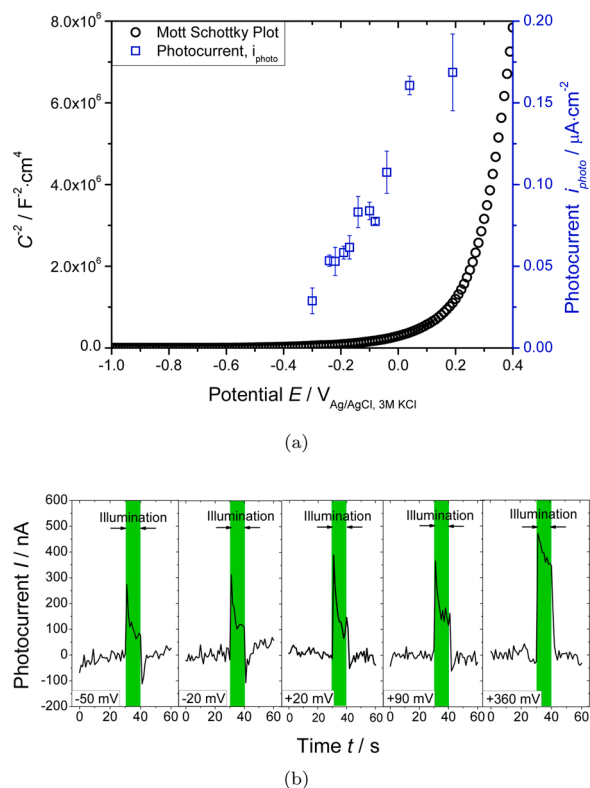


**Fig. 9.** (a) Mott-Schottky plots (squared capacitance  $C^2$  vs.  $E$ ) for 350 nm thick iron oxide in 0.1 M NaOH, and corresponding photocurrents at the different potentials. The OCP of the sample was  $-170$  mV vs. Ag/AgCl/3 M KCl. The photocurrent measurements indicate a flat band potential below  $-0.30$  V. (b) A selection of the photocurrent transients for 350 nm thick iron oxide in 0.1 M NaOH polarised relative to the OCP. Photocurrent transient at OCP are shown in Fig. 6a.

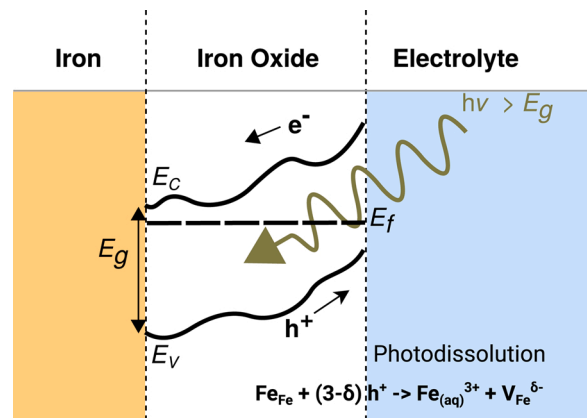


**Fig. 10.** Schematic band diagram, showing the bottom of a fluctuating conduction band  $E_C$ , the top of a fluctuating valence band  $E_V$ , schematically the Fermi level  $E_F$ , the band gap  $E_G$  and the main dissolution reaction for photocorrosion on oxide covered iron.

decrease with time until steady state. The decrease proceeded with a power law of  $(I(t) - I_0) \propto t^\alpha$ , with  $\alpha \approx 0.8$ . This exponent is not directly giving hints to the nature of the underlying process. For a diffusive process,  $\alpha \approx 0.5$  would intuitively be expected, but the results deviate from that. An initial current decrease has been observed in studies with illumination on the 10–100 ms time scale and was attributed to a cathodic back reaction via surface states within the band gap [34,56], which may possibly involve the generation of hydroxyl radicals [57].

For a decay on the time scale as observed here, charge carrier diffusion and migration in the electric field have been used as explanation in  $\text{TiO}_2$  [58]. The observed  $\alpha$  could be treated as a hint that several processes contribute to the decay. On the minute time scale, similar to our work, the surface donor density has been shown to increase with time in  $\text{TiO}_2$  [59,60]; the resulting donor accumulation at the surface of the semiconductor because of the electric field of the space charge layer has been identified as reason for an observed current decay. Electron-hole pair recombination on passive tungsten showed photocurrent transient with decay time of seconds [55].

Some previous studies reported the opposite photovoltage effect compared to the negative OCP shift under illumination as observed here [17,18,20,21]. Consequently, the resulting behaviour is not universal for all photocorrosion phenomena. It has been proposed [17,18,20,21] that the effect from illumination could be explained by a modified Gerischer semiconductor model, where the generated electron-hole pairs directly oxidise the metal substrate or create radicals that increase the corrosion rate. The results for anodised iron in this paper do not support a hypothesis where the holes interact with the metal substrate, as in that case the holes would have to migrate towards the oxide/electrolyte interface. A possible explanation for the differences is that the defect chemistry in the oxides investigated in other works led to a reversal of the band bending, e.g. because of doping by alloy elements. Especially for thin layers, and thus also near surfaces, the defect dominating the semiconductor properties may be different from the bulk defect as shown for copper oxides [61]. An alternative explanation is a contribution of the mechanism discussed in Section 4.2 in some of the previous studies, leading to the observed differences.

Summarising, electron-hole pair generation with hole annihilation by oxide dissolution (Fig. 10) is the main mechanism leading to photocorrosion under the conditions of this work. This mechanism would dominate  $\Delta i_{\text{corr}}^{(\text{photo})}$  for thick oxide or other corrosion product layers. “Thick” in this context refers to oxide layers thicker than  $\approx 1/10$  of the illuminating wavelength. If thick oxide layers cannot form, e.g. in acid where the oxide has a sufficient solubility, this photocorrosion mechanism is suppressed. Being related to a linear absorption process,  $\Delta i_{\text{corr}}^{(\text{photo})}$  is expected to scale linear with the illumination intensity. The band bending is the same as expected for the typical photoelectrochemical system, i.e. upward band bending for an n-type oxide.

The experimental results show that the thickness dependence is not trivial. For thicknesses of oxide films below 200 nm,  $\Delta i_{\text{corr}}^{(\text{photo})}$  normalised to the incident light’s power density is on the order of  $10\text{--}20 \text{ pA W}^{-1} (\text{nm oxide})^{-1}$ . This number was obtained by linearly fitting  $\Delta i_{\text{corr}}^{(\text{photo})}$  (d) for the lowest thicknesses in Fig. 4c and dividing it by the order of magnitude of the illumination power density of  $100 \text{ W cm}^{-2}$ . Current or voltage response can be fast, i.e. on a ms time scale or faster. OCP changes in both directions are possible compared to the situation in the dark.

#### 4.2. Heating-induced convection

When light interacts with a metal, light absorption always leads to heating, and local heating of the electrode may create a temperature gradient in the electrolyte which, in turn, induces thermal convection and therefore increased mass transport [19,24]. Increased mass transport due to heating can for several reasons not explain the results in this paper.

Firstly, there is only an insignificant temperature increase during the experiment; in relation with previous studies [15,19,24] the observed temperature increase of  $0.2^\circ\text{C}$  is not enough to explain the increased corrosion currents and dissolution rates observed here under illumination.

Secondly, the current response when illuminated during chronoamperometry was instantaneous, which indicates a quicker process than heat induced convection [24]. Additionally, the  $i_{\text{photo}}$  response was

potential dependent, which indicates a semiconductor photo-electrochemical effect, and not a thermal effect on  $O_2$  transport.

Thirdly, with the electrolyte flow regime as used in this work, the previous experiments [24] which served as control experiments for this study did not show any photoresponse.

Lastly, the cathodic part of the polarisation curves are approximately identical for the acidic curves when illuminated compared to the dark, which is unexpected if heating was contributing. Tafel slopes indicate the possible role of oxygen transport to the electrode as partly rate determining. Such transport should be increased by heating [24], but no such increase was observed.

There is no evidence that under the controlled convection conditions used in this study, increased mass transport due to surface heating contributes significantly to increased corrosion rates. A quantitative analysis of the details of the light-matter interaction here is challenging [62], and beyond the scope of this work.

A minor contribution of heating induced convection cannot be ruled out, but it does not dominate the photocorrosion rate. It is furthermore possible that the oxides themselves might be heated more than the measured  $0.2^\circ\text{C}$ . Thermal effects in the oxide will be discussed in Section 4.3.

Summarising, increased transport by induced convection due to temperature gradients has been described previously [24]. This mechanism is absent in the presence of controlled convection as used for the experiments described here;  $\Delta i_{\text{corr}}^{(\text{photo})}$  is related to the flow patterns forming near the interface. A detailed understanding of this mechanism required an understanding of the forming induced convection patterns near the surface. Controlling convection suppresses this mechanism. Based on the analysis presented previously for a similar illumination geometry [24],  $\Delta i_{\text{corr}}^{(\text{photo})}/i_{\text{corr}}^{(\text{dark})} \approx 1/3$ . Normalised to the incident illumination power density for the systems in acid with the highest observed  $i_{\text{corr}}^{(\text{dark})}$  in this work,  $\Delta i_{\text{corr}}^{(\text{photo})} \approx 300 \text{ nA W}^{-1}$  in the absence of forced convection. Transients from this mechanism can be slow, and stretch over the minute time scale [24]. OCP would always shift positively.

### 4.3. Thermal effects in the oxide film

In addition to the formation of electron-hole pairs and increased convection, additional effects must influence the photocorrosion of iron with thin oxide films, because for polished iron in alkaline environments,  $\Delta i_{\text{corr}}^{(\text{photo})} > 0$ , while  $i_{\text{photo}} = 0$  when illuminating the samples. This discrepancy cannot be easily explained by increased convection, as discussed in Section 4.2.

The absence of a photocurrent in the native oxide is attributed to the low thickness of few nm for native oxides [63], and strong disorder in the oxide: the layer is too thin and has a too short electron-hole pair lifetime to generate a measurable  $i_{\text{photo}}$ . The mechanism described in Section 4.1 via electron-hole pair formation is therefore in itself is not enough to explain  $\Delta i_{\text{corr}}^{(\text{photo})}$  when illuminating iron with only a native oxide;  $i_{\text{photo}} \approx 9 \text{ nA cm}^{-2}$  would only increase the corrosion current density by  $0.01 \mu\text{A cm}^{-2}$ , which is much lower than the observed  $\Delta i_{\text{corr}}^{(\text{photo})} = 0.47 \mu\text{A cm}^{-2}$ . Nevertheless, illumination increases the corrosion current density of iron in alkaline electrolytes, the native oxide is photoactive, and can generate measurable  $i_{\text{photo}}$  if grown thick enough. Therefore, illumination must have several effects on the native oxides, which in combination lead to the increased corrosion rate.

Firstly, metal oxide dissolution proceeding through reaction (2) may weaken the passivating properties of the thin oxide and thus causing a higher  $i_{\text{corr}}$ . Secondly, based on the polarisation curves, it is likely that the corrosion reaction is in a mixed regime (Section 4.4), being partly kinetically controlled. Heating of the oxide might increase the electron transfer rate, consequently increasing the corrosion current density. There is no direct evidence for surface heating, as it is difficult to measure or retard such a local event. It is, however, likely that

illumination would have such an effect. This thermal effect is different from the induced convection discussed in Section 4.2. Thirdly, it is possible that the separation of the generated electron-hole pairs modifies the electric field in the oxide, increasing vacancy movement through the oxide. A result could be higher corrosion rates through faster transport, as suggested by the PDM [9,12]. An indication for this effect might be the slow relaxation for the light-induced current transient at OCP. This relaxation disappears at high positive potentials as the electric field becomes dominated by the polarisation.

A more detailed study of these effects would be needed; it is, however, extremely challenging to separate different effects for oxide thicknesses below 10 nm. The discrepancies between  $\Delta i_{\text{corr}}^{(\text{photo})}$  and  $i_{\text{photo}}$  for the 250 nm oxide in alkaline solution may also be related to such thermal effects inside the oxide.

These additional effects likely occur in the anodised samples as well, but with the much larger photocurrents in this case, it is less obvious that additional effects contribute significantly to  $\Delta i_{\text{corr}}^{(\text{photo})}$ . The electric field would be smaller for thicker oxides as the same potential drop is “smeared out” over a larger oxide thickness. Also light absorption and thus heating is distributed to a larger extend over the oxide film and the metal.

Summarising, thermal effects in the oxide film, possibly caused by the effect of gradients on the defect chemistry or defect transport, are postulated to explain the discrepancy between  $i_{\text{photo}}$  and  $\Delta i_{\text{corr}}^{(\text{photo})}$  observed for polished iron in NaOH, i.e. iron with a thin native oxide film, and possibly also for some of the thicker oxides. The mechanism discussed in Section 4.1 cannot easily account for these differences. The nature of this mechanism and its dependence on characteristic parameters require more detailed studies.

### 4.4. Further aspects of the photocorrosion mechanism and quantification of the different contributions

There is no evidence for a photocatalytic effect on any of the cathodic processes. The shape of the polarisation curves for the illuminated samples and the dark samples is similar, however there is a small increase in current in the anodic part of the curves, leading to  $\Delta i_{\text{corr}}^{(\text{photo})} > 0$ . The differences in both cathodic and anodic apparent Tafel slopes and the corrosion potential is small enough that the standard deviation of the samples overlap. The increase in anodic current compares favourably with the  $i_{\text{photo}}$  found from the anodised iron samples, which also is anodic. For the polished iron samples there is no difference in the cathodic current, while the anodised samples show a decrease in cathodic current.

The apparent Tafel slopes obtained especially for active iron are much higher than typical for purely electrochemical reactions, where a single electron transfer with a typical symmetry coefficient of  $\approx 0.5$  yields a slope of  $120 \text{ mV dec}^{-1}$ , and several concurrent electron transfer steps yield lower Tafel slopes. A line parallel to the potential axis (with a Tafel slope of infinity) on the other hand indicates transport control. From the curves obtained here, we conclude that we are in a mixed regime, where both electrochemical reactions and a transport controlled process contribute to the cathodic branches. In these systems, hydrogen evolution reaction (HER) and oxygen reduction reaction are the typical cathodic processes, the former with a Tafel slope of  $120 \text{ mV dec}^{-1}$  [64] and the latter transport controlled in typical aqueous corrosion regimes. The measured Tafel slopes indicate that both processes contribute to the cathodic curves. Absence of an effect of illumination on the cathodic branches of the polarisation curves on active iron indicates absence of a photocatalytic effect on the HER, which is another circumstantial evidence for the absence of a strong involvement of oxyl radicals in the photocorrosion process. The decreased currents in the cathodic curves under illumination for several passive iron species may be attributed to charge transport through the oxide layer; oxides may also be reduced at the lowest potentials here.

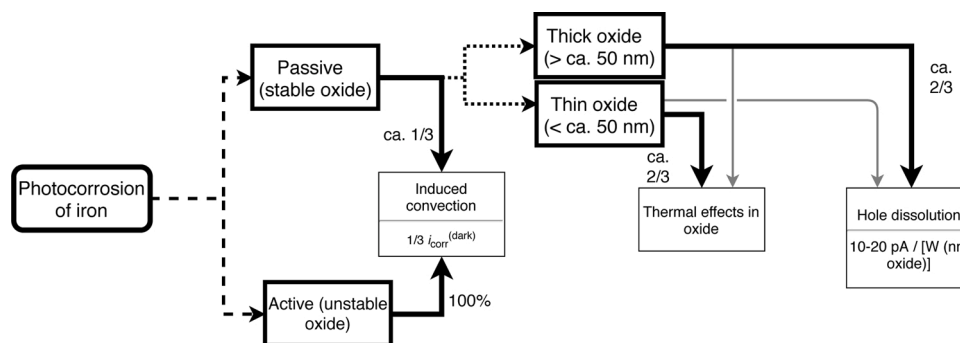


**Fig. 11.** Contributions of different mechanisms to the overall photocorrosion rate of iron based on the conditions used in this work. Results from Ref. [24] are also included. With oxide thickness, there is likely a transition between the hole dissolution and thermal effects in the oxide, indicated by the thick (main process) and thin (side process) arrows; side processes have not been quantified here.

In extension to the previously published works on photocorrosion [17,18,20–23], the scheme shown in Fig. 11 shows the different channels for photocorrosion discussed in Sections 4.1–4.4. Their different contributions have been quantified for the examples shown in this work, as indicated in Fig. 11, based on the results obtained here and previously [24].

## 5. Conclusion

Overall, three different mechanisms are found to contribute to the photocorrosion of iron, (i) electron–hole pair formation followed by  $\text{Fe}^{3+}$  ejection from the oxide, (ii) induced convection based on generation of temperature gradients in solution, and, as the former two contributions cannot quantitatively account for the total photocorrosion rates in passive iron with only a native oxide, (iii) thermal effects in the oxide film at the solid/liquid interface. The discussion from this work shows furthermore several features for the photocorrosion mechanisms discussed here, which can be used to validate the mechanism. Notably, the fraction of dissolving  $\text{Fe}^{3+}$  is expected to be higher in photocorrosion compared to “dark” corrosion of iron.

By anodising iron in alkaline solution, photoactive iron oxide layers with thicknesses of few tens to few hundreds of nanometres have been generated. The oxides, serving as defined models for corrosion products, behave as n-type semiconductors with direct band gap of 1.9–2.1 eV. When illuminated with photon energies above the band gap, at potentials above the flat band potential, photocurrents and photovoltages can be measured. Illumination also increases the corrosion rate of iron covered with such films, as well as for polished iron with its native oxide, in alkaline and neutral solution. For anodised iron, photocurrents are approximately the same as the observed increase in corrosion current, with the exception of one special thickness that shows the highest corrosion currents.

The results obtained here are clearly inconsistent with a picture of downward band bending in the semiconducting oxide. Photoelectrochemical experiments are consistent with an oxide layer with upward band bending at OCP. Electron–hole pair separation and thus the observation of photocurrents is difficult to explain without band bending. At the same time, a strong degree of band bending should also inhibit cathodic processes, as opposed to the observation. Therefore, it is clear that the band structure must be more involved in the system investigated here. A possible explanation for the observation of both increased anodic currents with low effect on cathodic currents are fluctuations — both spatial and temporal — in the band edges. The strong disorder in the iron oxides makes the presence of spatial fluctuations likely. Fluctuations on the order of the thermal energy  $k_B T$ ,  $\approx 25$  meV at room temperature, must anyway be accounted for. Therefore, fluctuations of few tens of millivolt on a band bending which is slightly larger can explain the observations from this work. (The alternative explanation of specially active cathodic areas is difficult to

rationalise in a uniform system as here). Oxide dissolution would thus occur by hole annihilation through cation ejection into the electrolyte. When the ejected cation originates from an iron ion on a lattice site, dissolution produces an iron vacancy. Alternatively, interstitial iron may dissolve. Illumination increases the fraction of iron that dissolves, as evidenced by concentration determination using UV–VIS spectroscopy. Increased dissolution is a sign of decreased oxide stability under illumination in alkaline solution.

The maximum increase in corrosion rate for the non-thermal effect was on the order of  $1 \mu\text{A cm}^{-2}$ , and can in most engineering application be ignored. Despite illumination with a powerful thermal white light source the differences between corrosion currents comparing illuminated an unilluminated samples is at maximum  $\approx 30\%$ . However, even slight differences in the uniform corrosion rate and the respective potentials can be important in the initiation of localised corrosion. In addition, if an iron oxide in contact with solution is exposed to strong illumination which is sustained over a long period of time, the accumulated effects may become substantial. These considerations may apply for photoelectrochemical water splitting, or photocathodic protection. The derived photocorrosion rates from this work should apply for iron oxide based photoanodes.

## Data availability

The raw and processed data required to reproduce these findings are available to download from NTNU’s institutional repository (<https://dataverse.no/ntnu>) via <https://doi.org/10.18710/CHYUQX>.

## Authors’ contribution

Håvard Wilson: data curation, investigation, formal analysis, visualisation, writing – original draft. Svein Sunde: methodology, supervision, validation, writing – reviewing and editing. Andreas Erbe: conceptualisation, methodology, resources, supervision, writing – reviewing and editing.

## Conflict of interest

None declared.

## References

- [1] C.H. Cribb, F.W.F. Arnaud, On the action of slightly alkaline waters on iron, *Analyst* 30 (1905) 225b–242, <https://doi.org/10.1039/AN905300225B>.
- [2] G.M. Enos, Fundamental factors in corrosion, *Ind. Eng. Chem.* 17 (1925) 793–797, <https://doi.org/10.1021/ie50188a006>.
- [3] L.C. Rowe, Effect of sunlight on the corrosion of steel, *Corrosion* 17 (1961) 267t–268t, <https://doi.org/10.5006/0010-9312-17.6.93>.
- [4] S. Wilhelm, K. Yun, L. Ballenger, N. Hackerman, Semiconductor properties of iron oxide electrodes, *J. Electrochem. Soc.* 126 (1979) 419–424, <https://doi.org/10.1149/1.2129055>.



- [5] S.M. Wilhelm, N. Hackerman, Photoelectrochemical characterization of the passive films on iron and nickel, *J. Electrochem. Soc.* 128 (1981) 1668–1674, <https://doi.org/10.1149/1.2127708>.
- [6] J. Bastidas, J. Scantlebury, Photopotentials and the corrosion of mild steel in sodium sulphate solution, *Corros. Sci.* 25 (1985) 377–382, [https://doi.org/10.1016/0010-938X\(85\)90036-8](https://doi.org/10.1016/0010-938X(85)90036-8).
- [7] J. Bastidas, J. Scantlebury, The influence of light on corrosion phenomena: the behaviour of mild steel in citric acid solution, *Corros. Sci.* 26 (1986) 341–347, [https://doi.org/10.1016/0010-938X\(86\)90009-0](https://doi.org/10.1016/0010-938X(86)90009-0).
- [8] T. Burleigh, C. Ruhe, J. Forsyth, Photo-corrosion of different metals during long-term exposure to ultraviolet light, *Corrosion* 59 (2003) 774–779, <https://doi.org/10.5006/1.3277606>.
- [9] D.F. Heaney, D.D. Macdonald, On the photoinhibition of passivity breakdown on iron in chloride-containing solutions, *J. Electrochem. Soc.* 146 (1999) 1773–1776, <https://doi.org/10.1149/1.1391841>.
- [10] P. Schmuki, H. Böhni, Illumination effects on the stability of the passive film on iron, *Electrochim. Acta* 40 (1995) 775–783, [https://doi.org/10.1016/0013-4686\(94\)00341-W](https://doi.org/10.1016/0013-4686(94)00341-W).
- [11] P. Schmuki, H. Böhni, Light induced inhibition of local passivity breakdown, *Mater. Sci. Forum* 185 (1995) 1065–1074, <https://doi.org/10.4028/www.scientific.net/MSF.185-188.1065>.
- [12] D.F. Macdonald, The point defect model for the passive state, *J. Electrochem. Soc.* 139 (1992) 3434–3449, <https://doi.org/10.1149/1.2069096>.
- [13] D.D. Macdonald, The history of the point defect model for the passive state: a brief review of film growth aspects, *Electrochim. Acta* 56 (2011) 1761–1772, <https://doi.org/10.1016/j.electacta.2010.11.005>.
- [14] M.G. Mahmoud, R. Wang, M. Kato, K. Nakasa, Influence of Ultraviolet Light Irradiation on Corrosion Behavior of Weathering Steel With and Without 1303-1308, 2015, <https://doi.org/10.1016/j.scriptamat.2005.07.039>.
- [15] A. Benedetti, L. Magagnin, F. Passaretti, E. Chelossi, M. Faimali, G. Montesperelli, Cathodic protection of carbon steel in natural seawater: effect of sunlight radiation, *Electrochim. Acta* 54 (2009) 6472–6478, <https://doi.org/10.1016/j.electacta.2009.06.0229>.
- [16] H. Riazi, I. Danaee, M. Peykari, Influence of ultraviolet light irradiation on the corrosion behavior of carbon steel AISI 1015, *Met. Mater. Int.* 19 (2013) 217, <https://doi.org/10.1007/s12540-013-2014-1>.
- [17] L. Song, Z. Chen, The role of UV illumination on the NaCl-induced atmospheric corrosion of Q235 carbon steel, *Corros. Sci.* 86 (2014) 318–325, <https://doi.org/10.1016/j.corsci.2014.06.013>.
- [18] L. Song, X. Ma, Z. Chen, B. Hou, The role of UV illumination on the initial atmospheric corrosion of 09CuPCrNi weathering steel in the presence of NaCl particles, *Corros. Sci.* 87 (2014) 427–437, <https://doi.org/10.1016/j.corsci.2014.07.013>.
- [19] A. Benedetti, C. Zanotti, P. Giuliani, M. Faimali, Non-isothermal effects induced by natural illumination and infrared irradiation on cathodically polarized carbon steel electrodes, *Corros. Sci.* 84 (2014) 125–134, <https://doi.org/10.1016/j.corsci.2014.03.022>.
- [20] P. Qiu, Z. Chen, H. Yang, L. Yang, L. Luo, C. Chen, The transformation of corrosion products on weathering steel by visible-light illumination under simulated marine atmospheric condition, *Int. J. Electrochem. Sci.* 11 (2016) 10498–10510, <https://doi.org/10.20964/2016.12.76>.
- [21] P. Qiu, H.F. Yang, L.J. Yang, Z.S. Chen, L.J. Lv, Y. Song, C.F. Chen, Enhanced inhibition of steel corrosion by L-cysteine under visible-light illumination, *Mater. Corros.* 68 (2017) 1004–1012, <https://doi.org/10.1002/maco.201609386>.
- [22] X. Qiu, J. Li, Z. Liu, Corrosion of weathering steel under light illumination and simulated atmospheric conditions, *Int. J. Electrochem. Sci.* 14 (2019) 3236–3244, <https://doi.org/10.20964/2019.04.36>.
- [23] L. Song, Z. Chen, Effect of  $\gamma$ -FeOOH and  $\gamma$ -Fe<sub>2</sub>O<sub>3</sub> on the corrosion of Q235 carbon steel under visible light, *J. Electrochem. Soc.* 162 (2015) C79–C84, <https://doi.org/10.1149/2.0301503jes>.
- [24] H. Wilson, A. Erbe, Convection induced by illumination-based metal surface heating increases corrosion potential, corrosion rates, *Electrochem. Commun.* 106 (2019) 106513, <https://doi.org/10.1016/j.elecom.2019.106513>.
- [25] M. Hanesch, Raman spectroscopy of iron oxides and (oxy)hydroxides at low laser power and possible applications in environmental magnetic studies, *Geophys. J. Int.* 177 (2009) 941–948, <https://doi.org/10.1111/j.1365-246X.2009.04122.x>.
- [26] G. Genchev, A. Erbe, Raman spectroscopy of mackinawite FeS in anodic iron sulfide corrosion products, *J. Electrochem. Soc.* 163 (2016) C333–C338, <https://doi.org/10.1149/2.1151606jes>.
- [27] M. Stratmann, J. Müller, The mechanism of the oxygen reduction on rust-covered metal substrates, *Corros. Sci.* 36 (1994) 327–359, [https://doi.org/10.1016/0010-938X\(94\)90161-9](https://doi.org/10.1016/0010-938X(94)90161-9).
- [28] S.L. Gojkovic, S. Zecevic, D. Drazic, Oxygen reduction on iron—Part VI. Processes in alkaline solutions, *Electrochim. Acta* 39 (1994) 975–982, [https://doi.org/10.1016/0013-4686\(94\)85115-8](https://doi.org/10.1016/0013-4686(94)85115-8).
- [29] T.W. Hamann, Splitting water with rust: hematite photoelectrochemistry, *Dalton Trans.* 41 (2012) 7830–7834, <https://doi.org/10.1039/C2DT30340J>.
- [30] A.G. Tamarit, J. Rick, A.A. Dubale, W.-N. Su, B.-J. Hwang, Using hematite for photoelectrochemical water splitting: a review of current progress and challenges, *Nanoscale Horiz.* 1 (2016) 243–267, <https://doi.org/10.1039/C5NH00098J>.
- [31] A.R.C. Bredar, A.L. Chown, A.R. Burton, B.H. Farnum, Electrochemical impedance spectroscopy of metal oxide electrodes for energy applications, *ACS Appl. Energy Mater.* 3 (2020) 66–98, <https://doi.org/10.1021/acsae.9b01965>.
- [32] H. Gerischer, The impact of semiconductors on the concepts of electrochemistry, *Electrochim. Acta* 35 (1990) 1677–1699, [https://doi.org/10.1016/0013-4686\(90\)87067-C](https://doi.org/10.1016/0013-4686(90)87067-C).
- [33] H. Wilson, S. Sunde, A. Erbe, Data Package For: Hole Annihilation vs. Induced Convection: Breakdown of Different Contributions to the Photocorrosion Mechanism of Oxide-Covered Iron, NTNU Open Research Data, NTNU, Trondheim, Norway, 2021, <https://doi.org/10.18710/CHYUQX>.
- [34] L. Abrantes, L. Peter, Transient photocurrents at passive iron electrodes, *J. Electroanal. Chem. Interf. Electrochem.* 150 (1983) 593–601, [https://doi.org/10.1016/S0022-0728\(83\)80238-1](https://doi.org/10.1016/S0022-0728(83)80238-1).
- [35] T. Burleigh, T. Dotson, K. Dotson, S. Gabay, T. Sloan, S. Ferrell, Anodizing steel in KOH and NaOH solutions, *J. Electrochem. Soc.* 154 (2007) C579–C586, <https://doi.org/10.1149/1.2767417>.
- [36] T. Burleigh, P. Schmuki, S. Virtanen, Properties of the Nanoporous Anodic Oxide, 2009, pp. C45–C53, <https://doi.org/10.1149/1.3021029>.
- [37] A.M. Jubb, H.C. Allen, Vibrational spectroscopic characterization of hematite, maghemite, and magnetite thin films produced by vapor deposition, *ACS Appl. Mater. Interfaces* 2 (2010) 2804–2812, <https://doi.org/10.1021/am1004943>.
- [38] R. Dieckmann, Defects and cation diffusion in magnetite (IV): nonstoichiometry and point defect structure of magnetite (Fe<sub>3–δ</sub>O<sub>4</sub>), *Ber. Bunsen-Ges. Phys. Chem.* 86 (1982) 112–118, <https://doi.org/10.1002/bbpc.19820860205>.
- [39] R. Dieckmann, C.A. Witt, T.O. Mason, Defects and cation diffusion in magnetite (V): electrical conduction, cation distribution and point defects in (Fe<sub>3–δ</sub>O<sub>4</sub>), *Ber. Bunsen-Ges. Phys. Chem.* 87 (1983) 495–503, <https://doi.org/10.1002/bbpc.19830870609>.
- [40] Y. Chen, P. Schneider, A. Erbe, Investigation of native oxide growth on zinc in different atmospheres by spectroscopic ellipsometry, *Phys. Status Solidi A* 209 (2012) 846–853, <https://doi.org/10.1002/pssa.201100542>.
- [41] Y. Chen, A. Erbe, In situ spectroscopic ellipsometry during electrochemical treatment of zinc in alkaline carbonate electrolyte, *Surf. Sci.* 607 (2013) 39–46, <https://doi.org/10.1016/j.susc.2012.08.006>.
- [42] A. Erbe, A. Sarfraz, C. Toparli, K. Schwenzfeier, F. Niu, Optical absorption spectroscopy at interfaces, in: P.R. Lang, Y. Liu (Eds.), *Soft Matter at Aqueous Interfaces*, Lect. Notes Phys., Springer, Cham, Switzerland, 2016, pp. 459–490, [https://doi.org/10.1007/978-3-319-24502-7\\_14](https://doi.org/10.1007/978-3-319-24502-7_14) (Chapter 2).
- [43] H. Pyenson, P. Tracy, A 1, 10-phenanthroline method for the determination of iron in powdered milk, *J. Dairy Sci.* 28 (1945) 401–412, [https://doi.org/10.3168/jds.S0022-0302\(45\)95191-5](https://doi.org/10.3168/jds.S0022-0302(45)95191-5).
- [44] R. Memming, *Semiconductor Electrochemistry*, 2nd ed., Wiley-VCH, Weinheim, Germany, 2015.
- [45] P. Searson, R. Latanision, U. Stimming, Analysis of the photoelectrochemical response of the passive film on iron in neutral solutions, *J. Electrochem. Soc.* 135 (1988) 1358–1363, <https://doi.org/10.1149/1.2095986>.
- [46] J.W. Schultze, A.W. Hassel, Passivity of metals, alloys, and semiconductors, in: A. Bard, M. Stratmann, G. Frankel (Eds.), *Encyclopedia of Electrochemistry*, vol. 4, Wiley-VCH, Weinheim, 2007, pp. 460–490 (Chapter 3.2).
- [47] A. Hankin, F.E. Bedoya-Lora, J.C. Alexander, A. Regoutz, G.H. Kelsall, Flat band potential determination: avoiding the pitfalls, *J. Mater. Chem. A* 7 (2019) 26162–26176, <https://doi.org/10.1039/C9TA09569A>.
- [48] F. Di Quarto, F. Di Franco, S. Miraghaei, M. Santamaria, F. La Mantia, The amorphous semiconductor Schottky barrier approach to study the electronic properties of anodic films on Ti, *J. Electrochem. Soc.* 164 (2017) C516–C525, <https://doi.org/10.1149/2.1709055es>.
- [49] H. Gerischer, On the interpretation of photoelectrochemical experiments with passive layers on metals, *Corros. Sci.* 31 (1990) 81–88, [https://doi.org/10.1016/0010-938X\(90\)90094-L](https://doi.org/10.1016/0010-938X(90)90094-L).
- [50] M. Reithmeier, A. Erbe, Dielectric interlayers for increasing the transparency of metal films for mid-infrared attenuated total reflection spectroscopy, *Phys. Chem. Chem. Phys.* 12 (2010) 14798–14803, <https://doi.org/10.1039/C0CP01125H>.
- [51] S. Nayak, P.U. Biedermann, M. Stratmann, A. Erbe, A mechanistic study of the electrochemical oxygen reduction on the model semiconductor n-Ge(100) by ATR-IR and DFT, *Phys. Chem. Chem. Phys.* 15 (2013) 5771–5781, <https://doi.org/10.1039/C2CP43909C>.
- [52] S. Nayak, P.U. Biedermann, M. Stratmann, A. Erbe, In situ infrared spectroscopic investigation of intermediates in the electrochemical oxygen reduction on n-Ge (100) in alkaline perchlorate and chloride electrolyte, *Electrochim. Acta* 106 (2013) 472–482, <https://doi.org/10.1016/j.electacta.2013.05.133>.
- [53] H. Gerischer, Electrochemical behavior of semiconductors under illumination, *J. Electrochem. Soc.* 113 (1966) 1174–1182, <https://doi.org/10.1149/1.2423779>.
- [54] H. Gerischer, Über den Mechanismus der anodischen Auflösung von Galliumarsenid, *Ber. Bunsenges. Phys. Chem.* 69 (1965) 578–583, <https://doi.org/10.1002/bbpc.19650690707>.
- [55] A. Goossens, D.D. Macdonald, A photoelectrochemical impedance spectroscopic study of passive tungsten, *J. Electroanal. Chem.* 352 (1993) 65–81, [https://doi.org/10.1016/0022-0728\(93\)80255-G](https://doi.org/10.1016/0022-0728(93)80255-G).
- [56] P. Iwanski, J. Curran, W. Gissler, R. Memming, The photoelectrochemical behavior of ferric oxide in the presence of redox reagents, *J. Electrochem. Soc.* 128 (1981) 2128–2133, <https://doi.org/10.1149/1.2127202>.
- [57] J. Curran, W. Gissler, The different photoelectrochemical behavior of sintered and flame-oxidized Fe<sub>2</sub>O<sub>3</sub>, *J. Electrochem. Soc.* 126 (1979) 56, <https://doi.org/10.1149/1.2128988>.
- [58] P.C. Searson, D.D. Macdonald, L.M. Peter, Frequency domain analysis of photoprocesses at illuminated semiconductor electrodes by transient transformation, *J. Electrochem. Soc.* 139 (1992) 2538–2543, <https://doi.org/10.1149/1.2221259>.
- [59] L. Harris, R. Wilson, Aging effects in single crystal reduced rutile anodes, *J. Electrochem. Soc.* 123 (1976) 1010–1015, <https://doi.org/10.1149/1.2132982>.
- [60] M. Butler, Aging effects in defect-doped semiconducting electrodes, *J. Electrochem. Soc.* 126 (1979) 338–341, <https://doi.org/10.1149/1.2129033>.



- [61] C. Toparli, A. Sarfraz, A.D. Wieck, M. Rohwerder, A. Erbe, In situ and operando observation of surface oxides during oxygen evolution reaction on copper, *Electrochim. Acta* 236 (2017) 104–115, <https://doi.org/10.1016/j.electacta.2017.03.137>.
- [62] M. Auinger, P. Ebbinghaus, A. Blümich, A. Erbe, Effect of surface roughness on optical heating of metals, *J. Eur. Opt. Soc. Rapid Publ.* 9 (2014) 14004, <https://doi.org/10.2971/jeos.2014.14004>.
- [63] S. Suzuki, Y. Ishikawa, M. Isshiki, Y. Waseda, Native oxide layers formed on the surface of ultra high-purity iron and copper investigated by angle resolved XPS, *Mater. Trans. JIM* 38 (1997) 1004–1009, <https://doi.org/10.2320/matertrans1989.38.1004>.
- [64] A.R. Zeradjanin, J.-P. Grote, G. Polymeros, K.J.J. Mayrhofer, A critical review on hydrogen evolution electrocatalysis: re-exploring the volcano-relationship, *Electroanalysis* 28 (2016) 2256–2269, <https://doi.org/10.1002/elan.201600270>.